

## Technical Note: Feasibility of CO<sub>2</sub> profile retrieval from limb viewing solar occultation made by the ACE-FTS instrument

P. Y. Foucher<sup>1</sup>, A. Chédin<sup>1</sup>, G. Dufour<sup>2</sup>, V. Capelle<sup>1</sup>, C. D. Boone<sup>3</sup>, and P. Bernath<sup>3,4</sup>

<sup>1</sup>Laboratoire de Météorologie Dynamique/Institut Pierre Simon Laplace, Ecole Polytechnique, 91128 Palaiseau, France

<sup>2</sup>Laboratoire Inter-universitaire des Systèmes Atmosphériques, Faculté des Sciences et Technologies, 61 avenue du Général de Gaulle, 94010 Créteil, France

<sup>3</sup>Department of Chemistry, University of Waterloo, Ontario, N2L3G1, Canada

<sup>4</sup>Department of Chemistry, University of York, Heslington, York, YO105DD, UK

Received: 29 September 2008 – Published in Atmos. Chem. Phys. Discuss.: 7 January 2009

Revised: 9 March 2009 – Accepted: 16 April 2009 – Published: 30 April 2009

**Abstract.** Major limitations of our present knowledge of the global distribution of CO<sub>2</sub> in the atmosphere are the uncertainty in atmospheric transport mixing and the sparseness of in situ concentration measurements. Limb viewing spaceborne sounders, observing the atmosphere along tangential optical paths, offer a vertical resolution of a few kilometers for profiles, which is much better than currently flying or planned nadir sounding instruments can achieve. In this paper, we analyse the feasibility of obtaining CO<sub>2</sub> vertical profiles in the 5–25 km altitude range from the Atmospheric Chemistry Experiment Fourier Transform Spectrometer (ACE-FTS, launched in August 2003), high spectral resolution solar occultation measurements. Two main difficulties must be overcome: (i) the accurate determination of the instrument pointing parameters (tangent heights) and pressure/temperature profiles independently from an a priori CO<sub>2</sub> profile, and (ii) the potential impact of uncertainties in the temperature knowledge on the retrieved CO<sub>2</sub> profile. The first difficulty has been solved using the N<sub>2</sub> collision-induced continuum absorption near 4 μm to determine tangent heights, pressure and temperature from the ACE-FTS spectra. The second difficulty has been solved by a careful selection of CO<sub>2</sub> spectral micro-windows. Retrievals using synthetic spectra made under realistic simulation conditions show a vertical resolution close to 2.5 km and accuracy of the order of 2 ppm after averaging over 25 profiles. These results open the way to promising studies of transport mechanisms and carbon fluxes from the ACE-FTS measurements.

First CO<sub>2</sub> vertical profiles retrieved from real ACE-FTS occultations shown in this paper confirm the robustness of the method and applicability to real measurements.

### 1 Introduction

Determining the spatial and temporal structure of surface carbon fluxes has become a major scientific issue during the last decade. In the so-called “inverse” approach, observed atmospheric concentration gradients are used to disentangle surface fluxes, given some description of atmospheric transport. This approach has been widely used to invert concentration measurements of CO<sub>2</sub> from global surface networks to estimate the spatial distribution of annual mean surface fluxes (Gurney, 2002) and their interannual variability (Baker, 2006). Major limitations of the inverse approach are the uncertainties in atmospheric transport and the sparseness of atmospheric CO<sub>2</sub> concentration measurements based on a network of about 100 surface stations unevenly distributed over the world. As a consequence, the number of CO<sub>2</sub> in situ observations, particularly from aircraft (research campaigns or regular aircraft measurements: see, e.g., Andrew (2001); Brenninkmeijer (1999); Matsueda (2002); Engel (2006) and references herein), has increased in recent years.

Although sporadic in time and space, in situ aircraft measurements are useful to test the modeling of the transport of air from the surface to the upper troposphere and lower stratosphere as well as the incursion of stratospheric air back into the upper troposphere. Since CO<sub>2</sub> is inert in the lower atmosphere, its long-term trend and pronounced seasonal cycle (due to the uptake and release by vegetation) propagate



Correspondence to: P. Y. Foucher  
([pierre-yves.foucher@lmd.polytechnique.fr](mailto:pierre-yves.foucher@lmd.polytechnique.fr))

from the surface, and the difference between atmospheric and surface mixing ratios is determined by the processes that transport surface air throughout the atmosphere, including advection, convection and eddy mixing (Shia, 2006). Because it takes several months to transport surface air to the lower stratosphere, the CO<sub>2</sub> mixing ratio is lower and the seasonal cycle is different there as compared to the troposphere (Plumb, 1992, 1996; Shia, 2006). However, the transport processes, and in particular small-scale dynamical processes, such as convection and turbulence associated with frontal activity, which cannot be explicitly resolved by chemistry-transport models in this region, are complex and our understanding is still poor. Bönisch (2008), evaluated transport in three-dimensional chemical transport models in the upper troposphere and lower stratosphere by using observed distributions of CO<sub>2</sub> and SF<sub>6</sub>. They show that although all models are able to capture the general features in tracer distributions including the vertical and horizontal propagation of the CO<sub>2</sub> seasonal cycle, important problems remain such as: (i) a too strong Brewer-Dobson circulation causing an overestimate of the tracer concentration in the Lower Most Stratosphere (LMS) during winter and spring, (ii) a too strong tropical isolation leading to an underestimate of the tracers in the LMS during winter. Moreover, all models tested suffer to some extent from diffusion and/or too strong mixing across the tropopause. In addition, the models show too weak vertical upward transport into the upper troposphere during the boreal summer.

In recent years it has become possible to measure atmospheric CO<sub>2</sub> from space. Satellite-based observations by the nadir-viewing vertical sounders TIROS-N Operational Vertical Sounder (TOVS), Atmospheric Infrared Sounder (AIRS) (Chédin, 2002, 2003a, b; Crevoisier, 2004; Engelen, 2005), or SCIAMACHY (Buchwitz, 2005), and now the Infrared Atmospheric Sounder Interferometer (IASI) have the potential to dramatically increase the spatial and temporal coverage of CO<sub>2</sub> measurements. In the January 2009, the Greenhouse gases Observing Satellite (GOSAT) mission has been launched to measure CO<sub>2</sub> and methane column densities from orbit. The satellite data products are all vertically integrated concentrations rather than the profile measurements that are essential to a comprehensive understanding of distribution mechanisms of CO<sub>2</sub>. The difference between the column-averaged CO<sub>2</sub> mixing ratio and the surface value varies from 2 to 10 ppmv depending on location and time of year (Olsen, 2004). The upper troposphere can contribute significantly to this difference because this portion of the column constitutes approximately 20% of the column air mass and the CO<sub>2</sub> mixing ratios in this region can differ by 5 ppmv or more from the CO<sub>2</sub> mixing ratios at the surface (Anderson, 1996; Matsueda, 2002; Shia, 2006). With limb sounders that observe the atmosphere along tangential optical paths, the vertical resolution of the measured vertical profiles is of the order of a few kilometers, much better than can be achieved with nadir sounding instruments. The At-

mospheric Chemistry Experiment Fourier Transform Spectrometer (ACE-FTS), launched in August 2003, is a limb sounder that records solar occultation measurements (up to 30 occultations each day) with coverage between approximately 85° N and 85° S (Bernath, 2005), with more observations at high latitudes than over the tropics (Bernath, 2006). The ACE-FTS has high spectral resolution (0.02 cm<sup>-1</sup>) and the signal-to-noise ratio of ACE-FTS spectra is higher than 300:1 over a large portion (1000–3000 cm<sup>-1</sup>) of the spectral range covered (750–4400 cm<sup>-1</sup>). Our analysis is organised as follows. We first present the method used to retrieve CO<sub>2</sub> profiles from limb viewing observations, the problems encountered in estimating the tangent heights of the measurements and the strategy adopted using the N<sub>2</sub> continuum absorption. We then discuss in detail the crucial step of selecting appropriate spectral regions to use in the retrievals (the so-called “micro-windows”). The micro-windows are optimized to provide the maximum amount of information on the target variables: instrument pointing parameters and CO<sub>2</sub> profiles. The selection procedure takes into account errors due to instrumental and spectroscopic parameters noise, to interfering species (species other than CO<sub>2</sub>) and to temperature uncertainties. Constraints on the estimator are then discussed in detail and results are presented on the degrees of freedom, the vertical resolution, the error and standard deviation of the retrieved profiles. Finally, results using synthetic spectra and first retrievals using real ACE-FTS data are presented and discussed.

## 2 Retrieving CO<sub>2</sub> profiles from limb viewing observations: problems and strategy

### 2.1 Instrument pointing

Interpreting limb viewing observations in terms of atmospheric variables requires accurate knowledge of instrument pointing parameters (tangent heights) and pressure/temperature (hereafter referred to as “pT”) vertical profiles. Temperature and tangent heights can be viewed as independent parameters whereas pressure can be calculated from temperature and altitude by using the hydrostatic equilibrium equation. Reactive trace gases are the usual target species of limb-viewing instruments, so pointing parameters are simultaneously retrieved with pT by the analysis of properly selected CO<sub>2</sub> lines under the assumption (questionable, in certain cases) of a weak variation of its atmospheric concentration around a given a priori value. In the stratosphere, pT and tangent height errors caused by a variation of the CO<sub>2</sub> mixing ratio is not the major source of error, and, for example, is about 10% of the total error as estimated for the MIPAS sounder for a CO<sub>2</sub> uncertainty of 3 ppm (von Clarmann, 2003). This approach becomes more problematic in the troposphere because: (i) the weak CO<sub>2</sub> lines used are more sensitive to an error in the assumed CO<sub>2</sub> concentration

(Park, 1997), and (ii) the variability in this concentration is much larger than in the stratosphere. Moreover, when the target gas is CO<sub>2</sub> itself, determining the pointing parameters from CO<sub>2</sub> lines is clearly impossible and would obviously introduce artificial correlations between the pointing and the CO<sub>2</sub> concentration. A critical step in this research has therefore been to develop a method of obtaining pT profiles and tangent heights independent of any a priori CO<sub>2</sub> knowledge. Only absorbing gases whose abundance is well known and constant can be used to achieve this goal.

In the case of ACE v2.2 retrieval (Boone, 2005), pT and tangent heights are fitted simultaneously using suitable CO<sub>2</sub> lines above 12 km; below 12 km, pT profiles are from the Canadian Meteorological Centre (CMC) analysis data, and tangent heights are fitted using CO<sub>2</sub> lines around 2600 cm<sup>-1</sup>. Above 12 km, the CO<sub>2</sub> lines used for ACE v2.2 retrieval are more sensitive to pointing parameters than to the CO<sub>2</sub> volume mixing ratio; however below 12 km the CO<sub>2</sub> lines around 2600 cm are very sensitive to the CO<sub>2</sub> concentration and the bias in the tangent heights due to the assumed CO<sub>2</sub> concentration increases dramatically. To determine tangent heights and pT profiles from ACE-FTS spectra that are independent of CO<sub>2</sub>, we make use of the N<sub>2</sub> absorption continuum (Lafferty, 1996). The possibility of employing the N<sub>2</sub> continuum in retrievals was mentioned in Boone (2005), but this paper represents the first time such a retrieval strategy has been implemented.

## 2.2 Retrieval strategy

The retrieval process has two main steps: pointing parameter estimation and then CO<sub>2</sub> vertical profile estimation. These retrievals both use a similar least-squares retrieval method. The target variable is a vector containing tangent heights and a temperature profile in the first step or a CO<sub>2</sub> profile in the second step. ACE-FTS measurements can be inverted to give the target variable using a least-squares retrieval method based on optimal estimation theory (Gelb, 1974; Rodgers, 2000) and a non-linear iterative estimator which minimizes the cost function:

$$\chi_i^2 = (\mathbf{y}_{\text{obs}} - \mathbf{y}(\mathbf{x}^i))^T \mathbf{S}_e^{-1} (\mathbf{y}_{\text{obs}} - \mathbf{y}(\mathbf{x}^i)) + (\mathbf{x}^i - \mathbf{x}_a)^T \mathbf{R}^{-1} (\mathbf{x}^i - \mathbf{x}_a) \quad (1)$$

where  $\mathbf{y}_{\text{obs}}$  is the measurement vector and  $\mathbf{y}(\mathbf{x}^i)$  the related computed forward model vector for the iterative step  $i$ ,  $\mathbf{x}^i$  is the target profile and  $\mathbf{x}_a$  its a priori value.  $\mathbf{S}_e$  is the random noise error covariance matrix. In order to take non-linearity into account, the following iterative process, from one state of the target profile to the next, is used (Levenberg, 1944; Marquardt, 1963; Rodgers, 2000):

$$\mathbf{x}^{i+1} - \mathbf{x}^i = (\mathbf{K}^T \mathbf{S}_e^{-1} \mathbf{K} + \mathbf{R} + \lambda \mathbf{D})^{-1} \times (\mathbf{K}^T \mathbf{S}_e^{-1} (\mathbf{y}_{\text{obs}} - \mathbf{y}(\mathbf{x}^i)) - \mathbf{R}(\mathbf{x}^i - \mathbf{x}_a)) \quad (2)$$

where  $\mathbf{K}$  is the  $n \times m$  Jacobian matrix containing the partial derivatives of all  $n$  simulated measurements  $\mathbf{y}(\mathbf{x})$  with respect to all  $m$  unknown variables  $\mathbf{x}$ :  $\mathbf{K}(u, l) = \frac{\partial \mathbf{y}(\mathbf{x})(u)}{\partial \mathbf{x}(l)}$  with  $(u, l) \in [1, n][1, m]$ , and  $\mathbf{R}$  is a regularization matrix. The term  $\mathbf{D}$  controls the “rate of descent” of the cost function in the least squares process. The scalar  $\lambda$  increases when the cost function is not reduced in a given iteration and decreases when the cost function decreases. Here the matrix  $\mathbf{D}$  is assumed diagonal and takes into account the possibility that the expected variance of each element of the state vector may be different:

$$\mathbf{D} = \text{diag}(\mathbf{K}^T \mathbf{S}_e^{-1} \mathbf{K} + \mathbf{R}) \quad (3)$$

The regularization matrix  $\mathbf{R}$  can take various forms, the simplest being a diagonal matrix containing the a priori inverse variance (if known) of the target variable. In a Bayesian sense, the inverse a priori covariance matrix  $\mathbf{S}_a^{-1}$  is the optimal choice for  $\mathbf{R}$  (Rodgers, 2000). However, when little information is available, a common choice is the use of a Tikhonov regularization (Tikhonov, 1963) with a squared and scaled finite difference smoothing operator (Twomey, 1963; Phillips, 1962; Steck, 2002). (see Sects. 3.2 and 4 for more details).

## 2.3 4A/OP-limb Radiative Transfer Model

The forward solution of the radiative transfer equation is provided by the 4A/OP-limb Radiative Transfer Model (RTM). 4A (for Automatized Atmospheric Absorption Atlas) is a fast and accurate line-by-line radiative transfer model (Scott, 1981) developed and maintained at Laboratoire de Météorologie Dynamique (LMD; see <http://ara.lmd.polytechnique.fr>) and was made operational (OP) in cooperation with the French company Noveltis (see <http://www.noveltis.net/4AOP> for a description of the 4A/OP version). 4A allows fast computation of the transmittance of discrete atmospheric layers (the nominal spectral grid is  $5 \times 10^{-4}$  cm but can be changed by the user), and of the radiance at a user-defined observation level. It relies on a comprehensive database (the atlases) of monochromatic optical thicknesses for up to 43 atmospheric molecular species. The atlases were created by using the line-by-line and layer-by-layer model, STRANSAC (Scott, 1974), in its latest 2000 version with up-to-date spectroscopy from the GEISA spectral line data catalog (Jacquinet-Husson, 2008). The 4A/OP-limb RTM also includes continua of N<sub>2</sub>, O<sub>2</sub> and H<sub>2</sub>O. For the present application, 4A/OP-limb uses new atlases suitable for a 1 km atmospheric grid spacing for the altitude range surface-100 km (100 levels). This 1 km discretization is used here for pressure, temperature and gas concentration profiles, as well as for the Jacobian calculations.

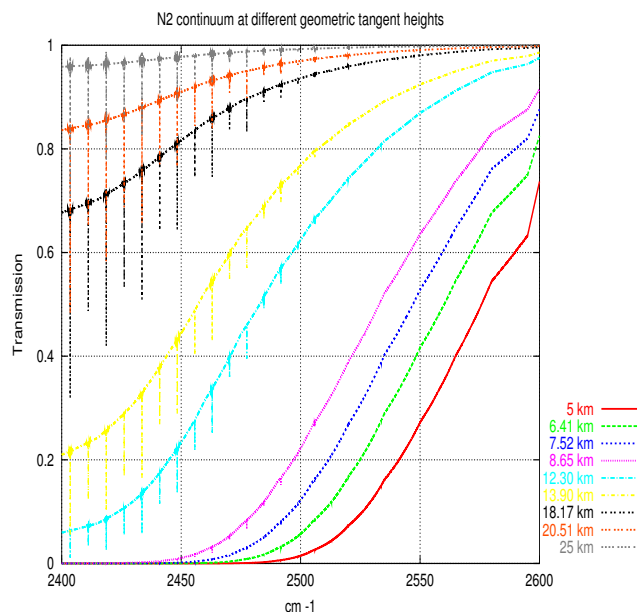


**Fig. 1.** Atmospheric N<sub>2</sub> continuum (and associated N<sub>2</sub> quadrupole lines) transmittance in the 2400–2600 cm spectral range for 9 geometric tangent heights from 5 km to 25 km from 4A/OP-limb RTM.

### 3 Spectral micro-window selection

#### 3.1 Spectral micro-window pre selection: a sensitivity analysis

To be selected and finally included in the measurement vector, a spectral micro-window must satisfy the obvious criteria of high sensitivity to the target variables (here the pointing parameters or CO<sub>2</sub>) and low sensitivity to non target variables. Investigations have to be carried out to analyze the quality of the spectral fit in order to minimize systematic contributions to the final error budget.

##### 3.1.1 Pointing parameters and the N<sub>2</sub> continuum absorption

As explained in Sect. 2, micro-windows are selected in the N<sub>2</sub> collision-induced absorption continuum near 4.0 μm to fit tangent heights and pT profiles in the 5–25 km altitude range. N<sub>2</sub> continuum absorption is significant for large optical paths obtained in the limb viewing geometry. 4A/OP-limb RTM uses an empirical model (Lafferty, 1996) determined from experimental data, which includes N<sub>2</sub>–N<sub>2</sub> and N<sub>2</sub>–O<sub>2</sub> collisions and covers the 190–300 K temperature range. Measurements cover the range 2125 cm (4.7 μm) to 2600 cm (3.8 μm) with a spectral resolution of 0.25 cm<sup>-1</sup>. N<sub>2</sub> continuum absorption becomes too weak to be used above 25 km and most of the band becomes saturated below 5 km; the atmospheric transmittance dynamic range is large in the 5–25 km altitude range as seen in Fig. 1. This spectral region

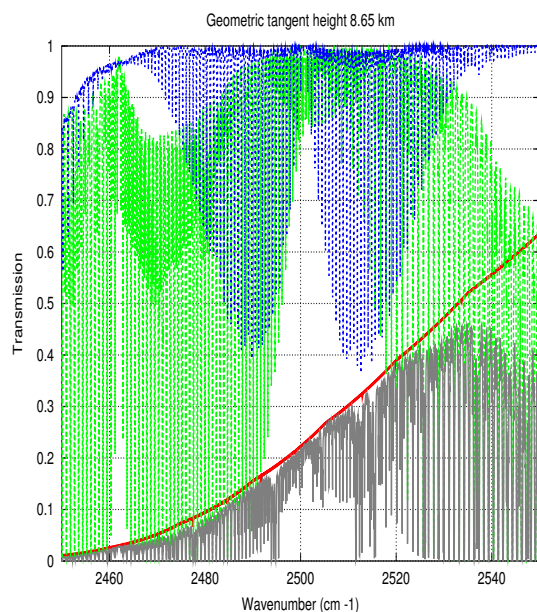


**Fig. 2.** Atmospheric transmittance in the 2450–2550 cm spectral range at 8.65 km (geometric tangent height) from 4A/OP-limb RTM. The N<sub>2</sub> continuum (and associated N<sub>2</sub> quadrupole lines) is represented in red. CO<sub>2</sub> and N<sub>2</sub>O absorptions are represented in blue and green, respectively. Total absorption is in grey.

also contains absorption from N<sub>2</sub>O and CO<sub>2</sub> lines. The far wing contributions from these molecules, which are difficult to model, may affect the baseline level in the vicinity of the N<sub>2</sub> continuum (see Figs. 2 and 3), thereby complicating the analysis. For wavenumbers below 2385 cm the spectrum is saturated up to 25 km due to CO<sub>2</sub> far wing absorption and the effect of this contribution on the N<sub>2</sub> baseline remains significant up to 2500 cm for the lowest altitudes and up to 2450 cm at 20 km. The contribution from N<sub>2</sub>O line wings is important for the lowest altitudes from 2400 cm to 2495 cm and from 2515 cm to 2600 cm but the N<sub>2</sub>O and CO<sub>2</sub> impact on the baseline rapidly decreases with increasing tangent height (see Fig. 3 for a geometric tangent height of 15.9 km). The geometric tangent height is the tangent altitude of the optical path without refraction. This geometric optical path is tangent to the true optical path (with refraction) at the satellite position. So, geometric tangent heights are always higher than true tangent heights. Figure 2 shows that at 8.65 km geometric tangent height (corresponding to a true tangent height around 7.7 km), CO<sub>2</sub> and N<sub>2</sub>O contributions to the N<sub>2</sub> absorption are only negligible in a small spectral region around 2500 cm<sup>-1</sup>, whereas at 15.90 km, Fig. 3 shows that a larger spectral region, from 2480 to 2520 cm<sup>-1</sup>, is available. In summary, the spectral ranges employed for pointing parameter retrieval using the N<sub>2</sub> continuum are as follows: 2495–2505 cm in the 5–10 km altitude range, 2490–2520 cm in the 10–15 km altitude range, 2480–2505 cm and around 2461 cm in the 15–25 km altitude range.

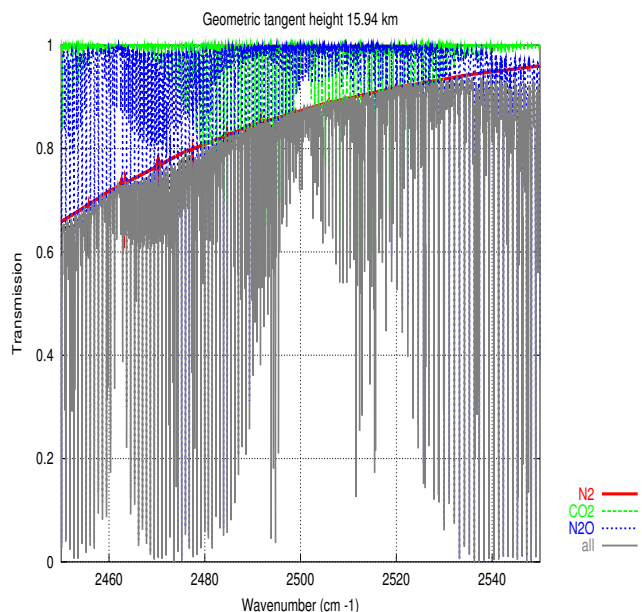


**Fig. 3.** Atmospheric transmittance in the 2450–2550 cm spectral range at 15.9 km (geometric tangent height) from 4A/OP-limb RTM. The N<sub>2</sub> continuum (and associated N<sub>2</sub> quadrupole lines) is represented in red. CO<sub>2</sub> and N<sub>2</sub>O absorptions are represented in blue and green, respectively. Total absorption is in grey.

The pure N<sub>2</sub> collision-induced absorption temperature dependence varies with wavenumber (Lafferty, 1996). Below 2450 cm<sup>-1</sup>, the absorption coefficient decreases with temperature, while the reverse is true for wavenumbers above 2450 cm<sup>-1</sup>; however the sensitivity to variations in tangent height is relatively constant throughout the continuum. To retrieve temperature and tangent height simultaneously above 12 km (see part 2.1), it is necessary to choose at least two different N<sub>2</sub> spectral micro-windows having different sensitivities to temperature, i.e., micro-windows around 2450 cm<sup>-1</sup> (or below) and micro-windows around 2500 cm<sup>-1</sup>. However, in the 2450 cm spectral range, absorption is very high below 10 km and is influenced by the N<sub>2</sub>O and CO<sub>2</sub> line far wings. In this paper we therefore focus mainly on tangent height retrievals although the results of a simultaneous fit are presented in part 5.

### 3.1.2 CO<sub>2</sub> concentrations: an analysis of CO<sub>2</sub> line sensitivity

The selection of CO<sub>2</sub> spectral micro-windows for both concentration and temperature retrievals is based on the analysis of 4A/OP-limb RTM simulated transmittances and Jacobians. In a first step, CO<sub>2</sub> lines with concentration Jacobians peaking within the tangent altitude range considered are selected. In a second step, CO<sub>2</sub> lines overlapped by other species are rejected on the basis of the relative importance

of the CO<sub>2</sub> Jacobian and the Jacobians of the other species. In a third step, only the CO<sub>2</sub> lines with a small lower state energy  $E''$  are selected to minimize the line intensity dependence on temperature. In fact, it may be shown that for a micro-window corresponding to a CO<sub>2</sub> line with a low value of the lower state energy  $E''$ , there exists a tangent height at which the temperature Jacobian is almost equal to zero (Park, 1997) and the sign of the temperature Jacobian is positive above this critical altitude and negative below.

Altogether, about 80 CO<sub>2</sub> micro-windows were pre-selected from five different spectral domains as shown in Table 3.1.2 (column 1: number of micro-windows; column 2: spectral domain and isotopologue). In this table they are classified according to the altitude range in which they are suitable for determining the CO<sub>2</sub> profile (column 3). Column 4 gives the average value of  $E''$  for the lines selected in each spectral domain. These values are much smaller than those corresponding to micro-windows traditionally selected for temperature retrieval when the target variable is not CO<sub>2</sub> (see column 5). Figures 4 and 5 show examples of pre-selected CO<sub>2</sub> micro-windows transmittances (Fig. 4) and sensitivities (Fig. 5), for each contributing species, versus wavenumber at a tangent height of 11.2 km. In Fig. 4, different situations are seen: (i) relatively clean CO<sub>2</sub> windows (b1, b2, b3, c2 and c3); (ii) windows with modest contributions from other species (O<sub>3</sub> in a3 and c1); windows with more pronounced signatures from other species (H<sub>2</sub>O in a1, O<sub>3</sub> in a2, CO in b4, and N<sub>2</sub>O in c4). The impact of other species, such as CH<sub>4</sub>, has also been tested (although no results are presented here). Figure 5 shows transmittance Jacobians for the same species and for the same CO<sub>2</sub> micro-windows. In this figure the temperature Jacobians are also plotted (black dashed line) which display different behaviours: positive sensitivity for a1, b1, and c3; negative sensitivity for a2, a3, b3, c1 and c2; sensitivity changing sign within the spectral interval for b4 and c4. Almost zero sensitivity is observed for b2. The expected presence of opposite temperature Jacobian signs, between 2030 cm and 2606 cm for example, is a very interesting point. Indeed, if two CO<sub>2</sub> lines with opposite temperature Jacobians for the same altitude range are used for CO<sub>2</sub> retrieval, the impact of temperature uncertainties on the retrieval in this altitude range is reduced (see part 3.2 on micro-windows optimization). When a micro-window is nearly free of absorption by other species, an easy method to select (or reject) the micro-window is to look at the ratio between its sensitivity to temperature to its sensitivity to CO<sub>2</sub>. The presence of an interfering species may be seen as a problem in terms of the error budget. However, this interference can lead to the temperature sensitivity changing sign within the micro-window (as in b4, for example) which may result in a less significant temperature sensitivity than for a cleaner micro-window with a more uniform (positive or negative) temperature sensitivity.

The instrumental noise, as well as the ability of the RTM to properly model the transmittance, also plays an important

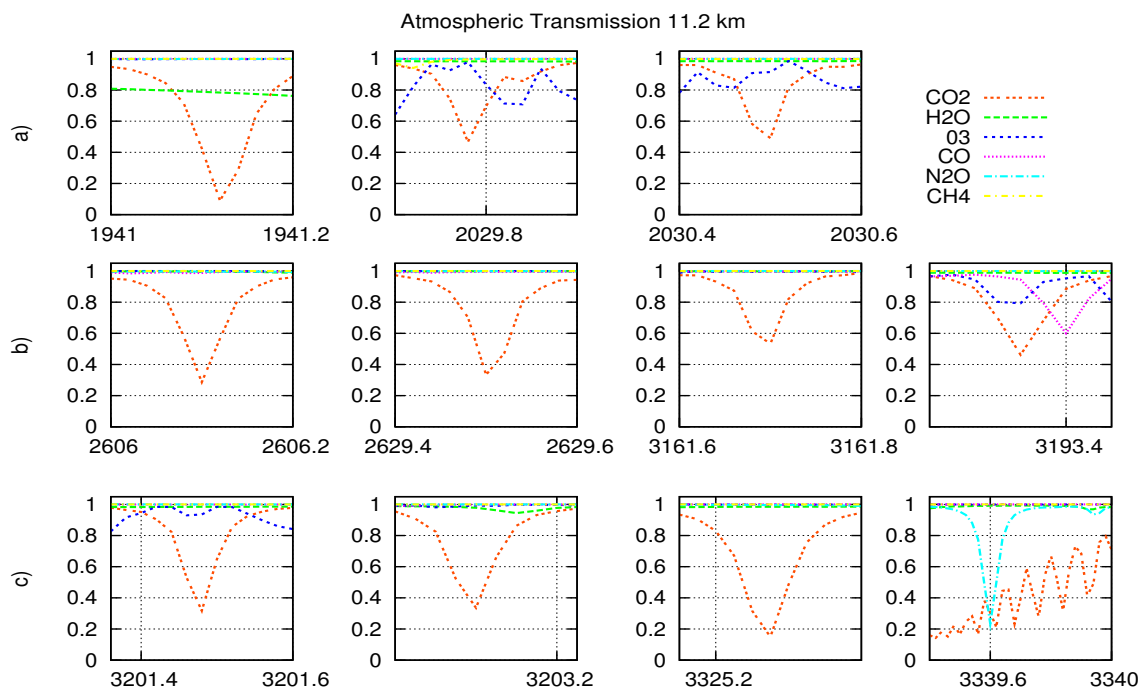


**Fig. 4.** Transmittance at 11.2 km versus wavenumber ( $\text{cm}^{-1}$ ) for 11 pre-selected CO<sub>2</sub> micro-windows (**a1** to **a3**, **b1** to **b4** and **c1** to **c4**, from left to right) with a spectral width of 0.2  $\text{cm}^{-1}$  (except **c4**). Each species contributing to the total absorption in the spectral range is identified by the colour legend (CO<sub>2</sub>: dotted red; H<sub>2</sub>O: dotted green, etc.).

role in the micro-window selection process: a “good” micro-window in term of sensitivity can be useless if the measurement or model errors are too large. Selecting an optimal set of micro-windows well distributed in the 5–25 km altitude range requires a detailed analysis of the retrieval error budget.

### 3.2 Optimization of the micro-window selection: error budget analysis

The total error budget on the target variable  $x$ ,  $\text{err}X(l)$ , at altitude level  $l$ , essentially results from the instrumental noise propagation error, error from parameter uncertainties (the effect of pT profiles and tangent height errors on CO<sub>2</sub> retrievals, for example), error uncertainties in other species, model and spectroscopic error. The  $\text{err}X(l)$  depends on the quality of the micro-window selection. Following von Clarmann (1998) and Dudhia (2002), the pre-selected micro-windows have been optimized by adjusting their boundaries and numbers so that the total retrieval error is minimized.

$$\text{err}X(l) = \sqrt{(\sigma(l) + \sum_j^p e^j(l)^2)} \quad (4)$$

$$e^j = (\mathbf{K}^T \mathbf{S}_e^{-1} \mathbf{K} + \mathbf{R})^{-1} \times \mathbf{K}^T \mathbf{S}_e^{-1} \mathbf{K}_j \Delta_j \quad (5)$$

$$\mathbf{S}_n = (\mathbf{K}^T \mathbf{S}_e^{-1} \mathbf{K} + \mathbf{R})^{-1} \times \mathbf{K}^T \mathbf{S}_e^{-1} \mathbf{K} \times (\mathbf{K}^T \mathbf{S}_e^{-1} \mathbf{K} + \mathbf{R})^{-1} \quad (6)$$

$$\sigma = \text{diag}(\mathbf{S}_n) \quad (7)$$

The total error budget  $\text{err}X(l)$  on the target variable is defined for altitude level  $l$  by Eq. (4) where  $\sigma(l)$  (Eq. 7) is the diagonal element of the random error propagation covariance matrix  $\mathbf{S}_n$  (Eq. 6),  $p$  is the number of non target parameters,  $e^j(l)$  (Eq. 5) is the error due to parameter  $j$  at level  $l$ , with  $\mathbf{K}_j$  the partial derivative of the corresponding transmittance matrix and  $\Delta_j$  the standard deviation vector of parameter  $j$  uncertainties.

Micro-window optimization requires the use of a regularization matrix, especially for CO<sub>2</sub>. Discussion of this constraint in terms of accuracy and vertical resolution is presented in part 4. In short, to optimize micro-windows, a first order finite difference Tikhonov regularization (see Sect. 2) is used to optimize temperature and tangent height micro-windows and a covariance matrix from the MOZART 3=D chemical transport model (Horowitz, 2003) is used to optimize CO<sub>2</sub> micro-windows. Note that the regularization does not modify the micro-window selection but is necessary to evaluate the total error budget.

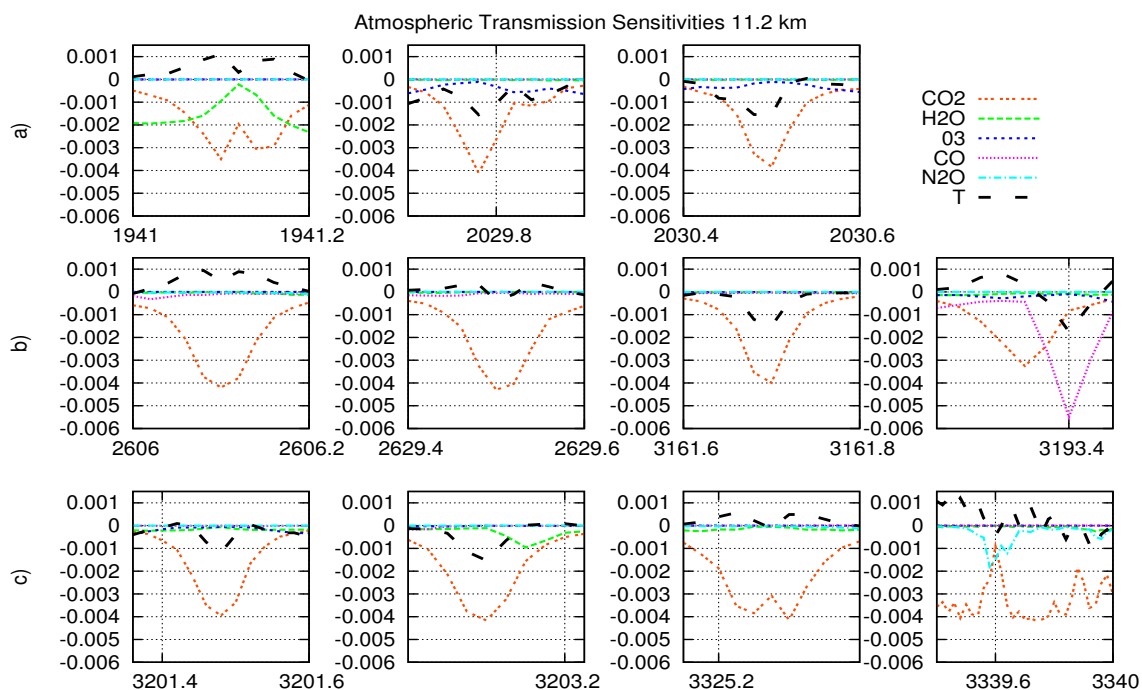


**Fig. 5.** Transmittance Jacobians at 11.2 km versus wavenumber ( $\text{cm}^{-1}$ ) for 11 pre-selected CO<sub>2</sub> micro-windows (**a1** to **a3**, **b1** to **b4** and **c1** to **c4**, from left to right) and for each species contributing to the total absorption in the spectral range, identified by the colour legend (CO<sub>2</sub>: dotted red; H<sub>2</sub>O: dotted green, etc.). Black dashed lines are for the temperature Jacobians. Species Jacobians other than CO<sub>2</sub> are for a 2% variation in their concentration; CO<sub>2</sub> Jacobians are for a variation of 5 ppm of its concentration; temperature Jacobians are for a variation of 1 K.

**Table 1.** CO<sub>2</sub> microwindow families.

number of mw	CO <sub>2</sub> spectral domain ( $\text{cm}^{-1}$ )	altitude range <sup>a</sup> (km)	$E''$ ( $\text{cm}^{-1}$ ) <sup>b</sup>	$E''$ ( $\text{cm}^{-1}$ ) <sup>c</sup>
12	1920–1955/ <sup>12</sup> C <sup>16</sup> O <sub>2</sub>	9–25	150.2	512.2
13	2010–2030/ <sup>13</sup> C <sup>16</sup> O <sub>2</sub>	7–20	162.8	
32	2600–2635/ <sup>18</sup> O <sup>16</sup> O	5–15	61.6	
9	3150–3205/ <sup>12</sup> C <sup>16</sup> O <sub>2</sub>	5–25	182.6	
16	3315–3355/ <sup>12</sup> C <sup>16</sup> O <sub>2</sub>	5–25	154.6	777.4

<sup>a</sup> not all microwindows of each family are used for the same altitude range

<sup>b</sup> mw used for CO<sub>2</sub> retrieval

<sup>c</sup> mw used for T retrieval

### 3.2.1 Optimized N<sub>2</sub> continuum micro-windows

For each spectral range available (see Sect. 3.1.1), optimum micro-windows are selected to minimize the CO<sub>2</sub> and N<sub>2</sub>O far wing contribution to the N<sub>2</sub> baseline continuum absorption and the retrieval error in general. Starting from a minimal width of 1 cm for an optimized micro-window, the total retrieval error is estimated as a function of the increasing width of the window. The random noise error, errors due to 5% percent changes in CO<sub>2</sub> and N<sub>2</sub>O concentrations,

and model errors due to CO<sub>2</sub> and N<sub>2</sub>O far wing contributions and N<sub>2</sub> continuum, estimated on the basis of comparisons with ACE-FTS measurements and experimental measurements (Lafferty, 1996), are taken into account in this analysis. The random noise variance used here is taken as twice the instrument noise variance to account for random errors from computation. Figure 6 shows the variation of the total error and of error components (random noise, CO<sub>2</sub>, N<sub>2</sub>O, model) as a function of the width of the micro-window for the spectral range around 2500  $\text{cm}^{-1}$ . These errors have

**Table 2.** Altitude retrieval error of selected N<sub>2</sub> microwindows.

N <sub>2</sub> spectral range (cm <sup>-1</sup> )	altitude range (km)	error (km)
2461.2–2462.8	15–20	70.10 <sup>-3</sup>
2504–2507	10–15	75.10 <sup>-3</sup>
2491.1–2493.1	12–17	65.10 <sup>-3</sup>
2498.5–2501.5	10–17	50.10 <sup>-3</sup>
2498–2502	5–10	40.10 <sup>-3</sup>

been averaged for tangent heights between 5 and 10 km. The initial micro-window width is 1 cm (50 spectral points) and its central wavenumber is 2500.7 cm<sup>-1</sup>, which corresponds to the centre of the CO<sub>2</sub> band (see Figs. 2 and 3). Then, step by step, 2 symmetric spectral points are added and the tangent height retrieval error is again estimated. From 1 cm to 9 cm width, the noise propagation error decreases from 25 m to 9 m, the model error increases from 35 m to 42 m, the error due to uncertainties in CO<sub>2</sub> and N<sub>2</sub>O concentration remains less than 5 m. The total error reaches its minimum value (about 40 m) at 3.5 cm width and remains approximately constant for larger widths. Similar results are obtained for the same spectral range for the 10–15 km altitude range (not shown). The total error comes to about 50 m; model error significantly increases with the width (due to CO<sub>2</sub> far wing model error as the N<sub>2</sub> continuum model error is quite constant in this spectral region); retrieval errors due to N<sub>2</sub>O and CO<sub>2</sub> concentration uncertainties remain low (less than 5 m). For this altitude range, in the spectral interval 2495–2505 cm<sup>-1</sup>, the optimal micro-window width is 3 cm<sup>-1</sup>. Results for the same altitude range in other spectral intervals, 2490–2495 cm and 2505–2520 cm<sup>-1</sup>, are also interesting. Optimized micro-windows resulting from this spectral analysis are presented in Table 2 for tangent height retrieval in the range 5–25 km.

### 3.2.2 Optimized set of CO<sub>2</sub> line micro-windows

In the case of CO<sub>2</sub>, many micro-windows may be considered for retrieving its concentration at a given altitude. Optimization of the set of pre-selected micro-windows is based on the evaluation of component and total errors due to noise propagation, temperature uncertainties, and, eventually, interfering species. The random noise introduced accounts for instrumental noise and CO<sub>2</sub> random spectroscopic parameters error. Resulting from comparisons between observations and model simulations, the transmittance model random error for CO<sub>2</sub> has been taken equal to  $0.5 \times 10^{-2}$  (i.e., twice as larger as instrumental random noise in the center of the band). Micro-window selection follows two main steps: (i) optimization of the width of each micro-window, (ii) creation of an optimum set of micro-windows.

For each pre-selected micro-window we first evaluate the impact of its spectral width on the retrieval error. Fig. 7a to

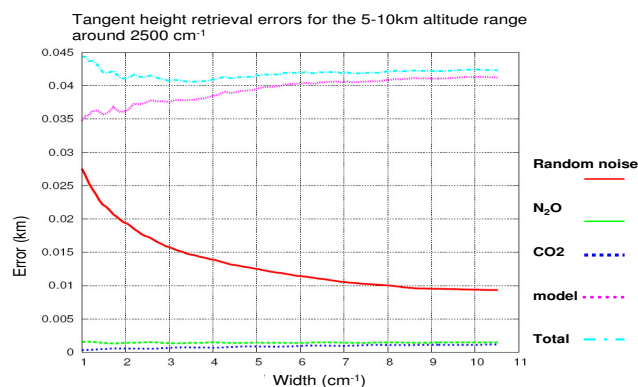


**Fig. 6.** Tangent height retrieval errors (in km) for the 5–10 km altitude range as a function of the micro-window width (cm<sup>-1</sup>). Micro-window centred at 2500.7 cm<sup>-1</sup>. Red: random noise error; blue and green: errors due to uncertainties on CO<sub>2</sub> and N<sub>2</sub>O, respectively; pink: model error due to N<sub>2</sub> continuum uncertainty, CO<sub>2</sub> and N<sub>2</sub>O far wing contributions; blue: total error.

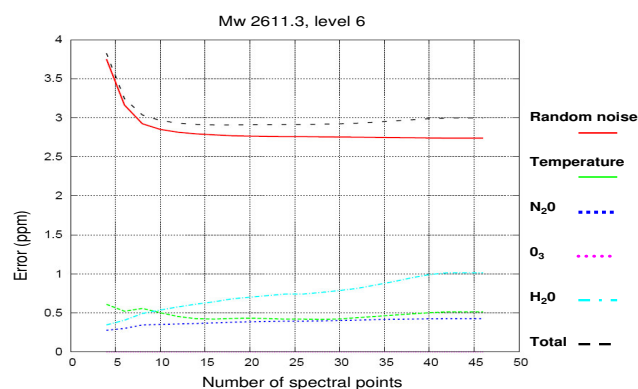


**Fig. 7a.** CO<sub>2</sub> retrieval errors (in ppm) for level at 6 km as a function of the micro-window number of spectral points (spectral step=0.02 cm<sup>-1</sup>). Micro-window centred at 2611.3 cm<sup>-1</sup>. Red: random noise error; blue, pink and pale blue: errors due to uncertainties on N<sub>2</sub>O, O<sub>3</sub> and H<sub>2</sub>O, respectively; dark: total error.

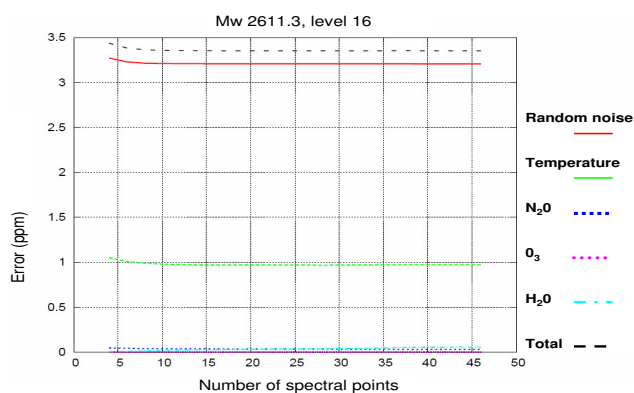
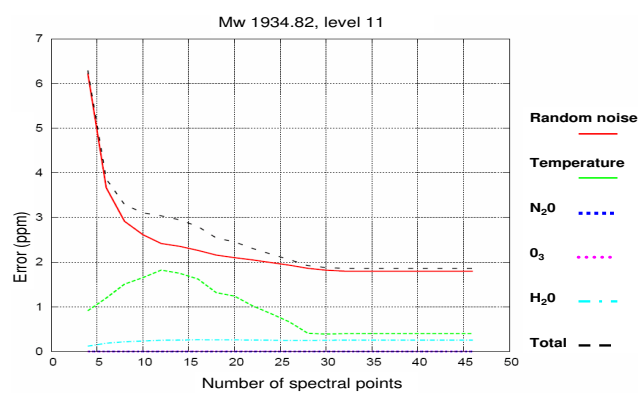
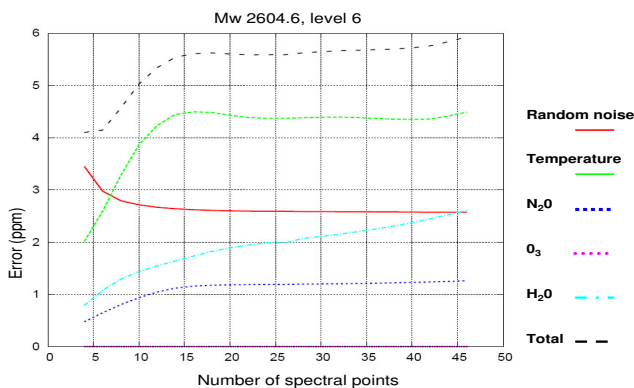
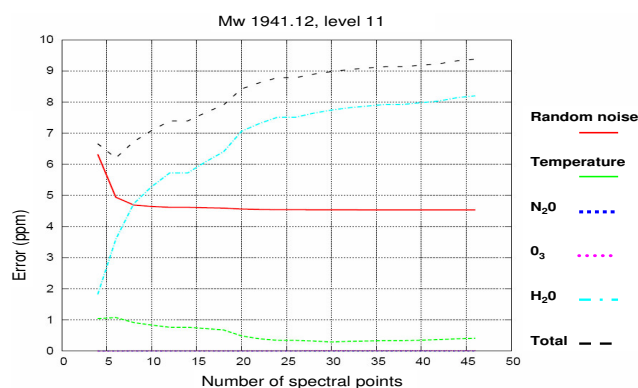
7e show retrieval error evolution with micro-window width for 4 different micro-windows at different tangent heights. Usually there is a significant decrease in noise propagation error with the width as seen in Fig. 7a, however interfering species error and temperature error evolution with width is not monotonic (see Fig. 7d) and depends on the altitude (see Fig. 7a and Fig. 7b). The optimal width of a micro-window increases when altitude decreases in order to reduce as much as possible noise error propagation. An interesting point is that interfering species can sometimes make temperature error decrease (see Fig. 7d). Finally, for each altitude, pre-selected width-optimized micro-windows are ranked according to their total error or rejected if the total error cannot be

**Table 3.** CO<sub>2</sub> error budget evolution as a function of the number of micro-windows selected.

Number of mw	Noise error <sup>a</sup>			Temperature error <sup>a</sup>			Total error <sup>b</sup>		
	5–10 km	10–15 km	15–20 km	5–10 km	10–15 km	15–20 km	5–10 km	10–15 km	15–20 km
10	0.759	0.746	0.742	0.694	0.789	0.397	0.738	0.805	0.723
15	0.499	0.573	0.578	0.277	1.18	0.663	0.440	0.702	0.585
20	0.409	0.479	0.480	0.363	1.03	0.437	0.394	0.601	0.477
25	0.378	0.451	0.436	0.177	0.892	0.757	0.324	0.547	0.464
30	0.365	0.421	0.423	0.365	0.959	0.857	0.388	0.582	0.467

<sup>a</sup> ratio between retrieval error and retrieval error from the initial set containing 5 micro-windows

<sup>b</sup> in ratio as <sup>a</sup>, total error includes random noise, temperature and non target species uncertainty errors

**Fig. 7b.** Same as Fig. 7a and for level at 16 km.**Fig. 7d.** Same as Fig. 7a for micro-window centred at 1934.8 cm and for level at 11 km.**Fig. 7c.** Same as Fig. 7a for micro-window centred at 2604.1 cm and for level at 6 km.**Fig. 7e.** Same as Fig. 7a for micro-window centred at 1941.1 cm and for level at 11 km.

reduced (see Fig. 7c and e). The optimal width varies from 0.2 cm to 0.6 cm with the micro-window and the altitude.

The second step of the optimization procedure consists of starting from a first “best set” of 5 micro-windows chosen among the micro-windows with lowest total error and well distributed within the 5–25 km altitude range. From this first

set, the number of micro-windows is progressively increased by adding windows of good quality (total error) while observing their impact on the total error.

Table 3.2.1 gives, for five augmented sets of micro-windows (column 1), the ratio between the

corresponding total error and that obtained with the original 5-micro-window set. Regarding the random noise error (columns 2–4), the retrieval error decreases when the number of micro-windows increases at each altitude range. A limit is reached for the set with 30 micro-windows. Temperature error (columns 5–7) behaviour varies with the altitude range: (i) in the 5–10 km altitude range the error decreases up to the 15 micro-windows set and then fluctuates with a minimum for the 25 micro-windows set, this being due to the fact that, for this altitude range, the temperature sensitivity sign frequently changes from one micro-window to another, leading to error compensation; (ii) in the 10–15 km altitude range the temperature sensitivity sign is more stable with slightly larger values for the augmented sets than for the initial 5-micro-window set: this set has been optimized to reduce temperature error in this altitude range; (iii) the 15–20 km altitude range error values are lower than for the initial 5-micro-window set with some important fluctuations with a minimum for the 10-micro-window set and a maximum for the 30-micro-window set. The total retrieval error (column 8–10) includes random noise, temperature and non target species uncertainty errors. It decreases when the number of micro-windows increases and validates this second step of the optimization process. However, from the 25 to the 30 micro-window set, the total error slightly increases at each altitude range: adding more pre selected micro-windows no longer improves the retrieval performance. Indeed, the noise error reaches its limit and the temperature error begins to increase significantly at each altitude range. The optimal 25-micro-window set is used in the following analysis.

#### 4 Retrieval error analysis: accuracy and vertical resolution

The choice of an appropriate regularization matrix  $\mathbf{R}$  (see Sect. 2.2), which may either smooth the retrieval or constrain its final state towards an a priori known state, has a direct impact on the retrieval error as it governs the balance between the information brought by the signal and that brought by the constraint.

##### 4.1 Choice of the regularization matrix $\mathbf{R}$

As stated in Sect. 2, one of the best choices for  $\mathbf{R}$  is the inverse a priori CO<sub>2</sub> covariance matrix  $\mathbf{S}_a$ , provided it is known accurately enough. Here,  $\mathbf{S}_a$  and associated a priori profiles  $\mathbf{x}_a$  have been calculated by the MOZART-CTM version 2 (Horowitz, 2003). These a priori matrices and profiles have been estimated for each season, and for five latitude bands (from  $-90^\circ$  to  $+90^\circ$  by  $30^\circ$ ) covering all longitudes. Diagonal elements of  $\mathbf{S}_a$  represent the expected variance of the CO<sub>2</sub> mixing ratio at each altitude and non diagonal elements represent the vertical correlation between CO<sub>2</sub> mixing ratios

**Table 4.** CO<sub>2</sub> retrieval degrees of freedom for the 5–20 km altitude range as a function of  $\alpha$ .

$df$	$\alpha$
8	$2.165 \times 10^{-3}$
9	$8.50 \times 10^{-4}$
10	$4.05 \times 10^{-4}$

at different altitudes. However, the impact of such a constraint on the retrieval is quite strong due to the presence of significant noise and the regularisation matrix  $\mathbf{R}$  is often assumed to be equal to the product  $\alpha \mathbf{S}_a^{-1}$ , where  $\alpha$  is a scalar less than unity. The optimized value of  $\alpha$  for the retrieval must ensure a good vertical resolution and a good accuracy. In the case of tangent height retrievals, we use a first order Tikhonov regularization as no covariance a priori data are available.

##### 4.2 Averaging kernel

The instrument has an input aperture of 1.25 mrad, which subtends an altitude range of 3–4 km at the tangent point. However, the altitude spacing between two sequential measurements in the 5–25 km range varies from about 3 km to less than 1 km and suggests that the effective vertical resolution of the ACE-FTS can be better than the field-of-view limit (Hegglin, 2008) if, for example, some deconvolution technique is used. For the purposes of this study, we will define the vertical resolution using the averaging kernel matrix,  $\mathbf{A}$ , and our analysis does not explicitly include the effect of the finite field-of-view of the instrument. To estimate the vertical resolution of the retrieval we use the averaging kernel matrix  $\mathbf{A}$  written as:

$$\mathbf{A} = (\mathbf{K}^T \mathbf{S}_e^{-1} \mathbf{K} + \mathbf{R})^{-1} \times \mathbf{K}^T \mathbf{S}_e^{-1} \mathbf{K} = \frac{\partial \hat{\mathbf{x}}}{\partial \mathbf{x}} \quad (8)$$

$$df = \text{tr}(\mathbf{A}) \quad (9)$$

$\mathbf{A}$  is the averaging kernel matrix,  $\hat{\mathbf{x}}$  is the retrieved profile and  $\mathbf{x}$  is the input profile: the  $k^{\text{th}}$  element of row  $j$  of the averaging kernel matrix represents the sensitivity of level  $j$  of the retrieved profile  $\hat{\mathbf{x}}$  to a 1 ppm change in the CO<sub>2</sub> mixing ratio of level  $k$  of the input profile  $\mathbf{x}$ . The trace of the averaging kernel matrix,  $df$  (Eq. 9), is equal to the degrees of freedom of the retrieval. When no constraint is applied, the averaging kernel is the identity matrix and the degrees of freedom of the retrieval is equal to the number of grid levels: the vertical resolution would here be equal to 1 km. Assuming a vertical resolution of about 2 km, corresponding to an average number of nine ACE-FTS measurements in the 5–25 km altitude range, the expected degrees of freedom for the retrieval comes to 9 which corresponds to an initial value of alpha of the order of  $8.5 \times 10^{-4}$ .

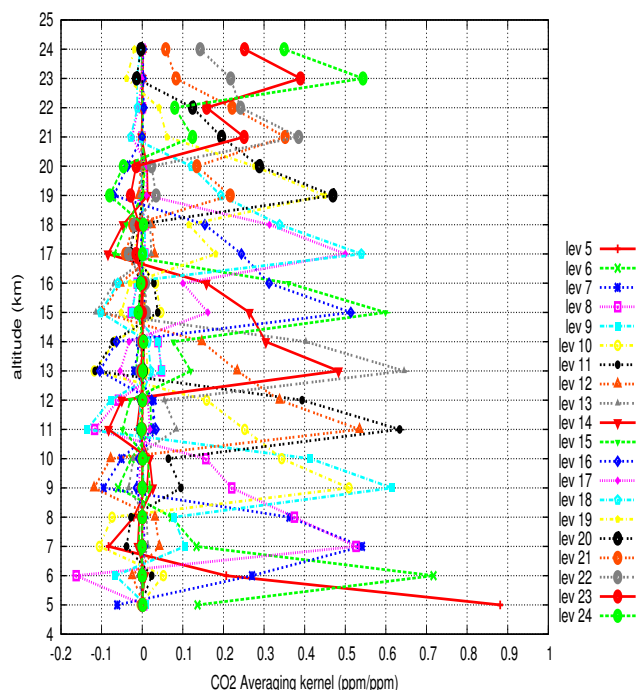


**Fig. 8.** Averaging kernel (row of **A**) for a retrieval degree of freedom equal to 9. Each curve labelled  $l$  on the right color legend represents the sensitivity, given in abscissa in ppm of CO<sub>2</sub>, of the retrieval at level  $l$  to a 1 ppm change made at the altitude (in km) given in ordinate. Each row of **A** corresponds to a retrieval level and to a coloured curve as indicated by the colour legend on the right. For example, the red curve labelled “lev 15” in this legend represents the sensitivity, given in abscissa in ppm of CO<sub>2</sub>, of the retrieval at level 15 (15 km altitude) to a 1 ppm change made at altitude given in ordinate.

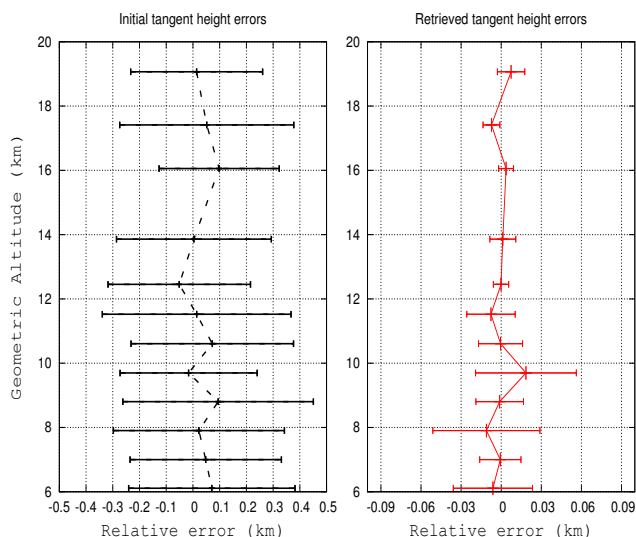
### 4.3 Vertical resolution

Figure 8 illustrates the averaging kernel for a degree of freedom of 9. For this example, level 15 averaging kernel values at altitude 15 km are slightly larger than 0.6. The maximum of level  $l$  averaging kernel generally occurs at altitude  $l$  and the vertical resolution corresponds to the half-width of the sensitivity distribution. For example, the vertical resolution of level 15 retrieval is close to 2 km. Figure 8 also shows that the peaks of the sensitivity distributions do not always correspond to the altitude at which the 1 ppm change has been made. For example, “lev 8”, “lev 10” and “lev 12” curves peak, respectively, at altitudes 7 km, 9 km and 11 km and their peak values are smaller than those of “lev 7”, “lev 9” and “lev 11” peaks and their associated vertical resolution is worse (around 3 km instead of 2 km). This means that retrievals are (respectively) more sensitive to changes at altitudes 7 km, 9 km and 11 km than at 8 km, 10 km and 12 km. This difference simply comes from the fact that the retrieval grid is finer than the measurement grid. Measurement tangent heights

(measurement grid) are closer, in this case, to the retrieval grid at altitudes 7 km, 9 km and 11 km than at 8 km, 10 km and 12 km altitudes. As expected, the retrievals are more sensitive near the observed tangent heights. Peak values are always larger than 0.5 (except in the 20–25 km altitude range), which confirms that the retrieval has been made using information primarily from the measurements rather than from the regularization (Koner, 2008) and that the retrieval grid of 1 km is adapted to the measurements. The decrease in the vertical resolution seen in the 20–25 km altitude range is due to a lack of CO<sub>2</sub> lines sufficiently sensitive to CO<sub>2</sub> concentration and sufficiently insensitive to temperature. As a consequence, averaging kernel peak values decrease. Above 20 km, information preferentially comes from the a priori vector.

### 4.4 Impact of the constraint on the retrieval error

To quantify the impact of the constraint on the retrieval error and to determine the best  $\alpha$  value, we carried out retrievals on synthetic spectra taking into account instrumental noise and an uncertainty in atmospheric temperature with no bias and a standard deviation of 1 K (random noise). A set of 25 synthetic occultations were generated using a common “true” CO<sub>2</sub> profile and different patterns for the random noise. CO<sub>2</sub> profiles are retrieved from each of these synthetic occultations. We performed the retrievals using different values of  $\alpha$  around the initial pre selected value corresponding to 9 degrees of freedom. The choice of an optimized  $\alpha$  is based on the calculation of the standard deviation between the mean retrieved profile and the true profile averaged over the altitude range 5–25 km (“accuracy”) and the standard deviation of the sample of 25 retrieved profiles (again 5–25 km average; “precision”). First, an important difference is seen between the “accuracy” and the “precision” results. This is due to spurious oscillations of the retrieved profiles around the true profile: they mostly compensate each other in the “accuracy” result whereas they clearly appear in the “precision” result for the lowest value of  $\alpha$ . For higher values of  $\alpha$ , the mean retrieved profile tends to a priori with no more spurious oscillations, the mean total error increases whereas the standard deviation decreases. Results of this analysis lead to degrees of freedom between 8 and 9, corresponding to a value of alpha of 0.001 (we have verified that, applied to real occultations, this value of  $\alpha$  actually minimizes the measurement part of the residual (first term of the right hand side of Eq. 1).



**Fig. 9a.** Single tangent height retrieval from N<sub>2</sub> continuum spectral windows in the 5–20 km altitude range using ACE level 2.2 temperature profile: results from 25 synthetic tests. Mean initial tangent height statistics (left): bias in dotted dark line and standard deviation (dark error bars). Mean retrieved tangent height statistics (right): bias in dotted red line and standard deviation (red error bars).

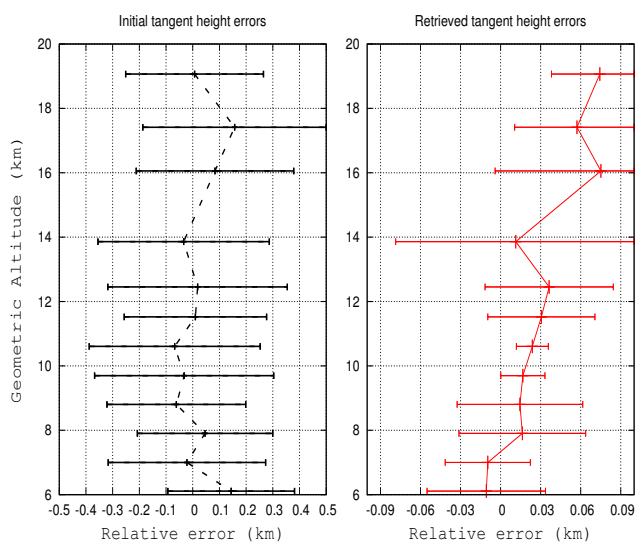


**Fig. 9b.** The same as Fig. 9a with 1 K bias and 1 K random noise added to the ACE level 2.2 temperature profile.

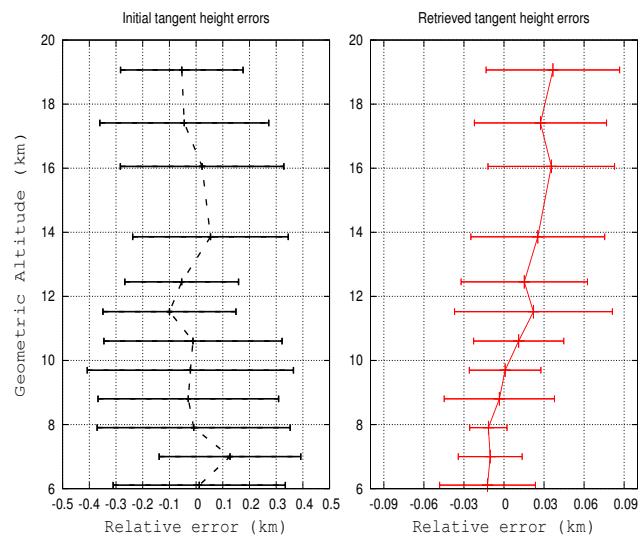


**Fig. 9c.** The same as Fig. 9b with simultaneous tangent height and temperature retrieval.

## 5 Application to real data, results and discussion

### 5.1 Tangent height

#### 5.1.1 Discussion of synthetic tests

Following the procedure described in Sect. 3, tangent height N<sub>2</sub>-retrievals on synthetic occultations have been carried out taking into account various options for the instrumental noise and an initial guess tangent height standard deviation of 0.3 km with no bias. Figure 9a (left) shows initial guess statistics (mean: dotted line; standard deviation: solid bars) over the 25 cases used in Sect. 4.4). Figure 9a (right), which assumes knowledge of the temperature, here from ACE v2.2 data, shows the mean tangent height retrieval error statistics: the standard deviation error (solid bars) is less than 20 m with almost no bias. For these synthetic tests, no model errors were introduced; consequently, an error of about 50 m (see Table 2) due to model uncertainties must be added to this result. Figure 9b shows similar results when knowledge of the temperature profile is not assumed: an uncertainty with a 1 K random error and a 1 K bias is introduced. On Fig. 9b (right), we see resulting tangent height biases varying with altitude: –10 m below 8 km, +30 m between 8 and 14 km and +70 m above. Standard deviations are larger, up to 100 m at 14 or 16 km. As mentioned in Sect. 3.1.1, simultaneous tangent height and temperature retrieval in principle requires the use of two different N<sub>2</sub> micro-windows to ensure stability. However, using the set of micro-windows of Table 2, Fig. 9c shows results corresponding to the same case as Fig. 9b (uncertainty of 1 K and bias of 1 K on temperature): the simultaneous fit reduces tangent height biases by a factor of about 2 above 14 km. Assuming ACE v2.2 errors on temperature

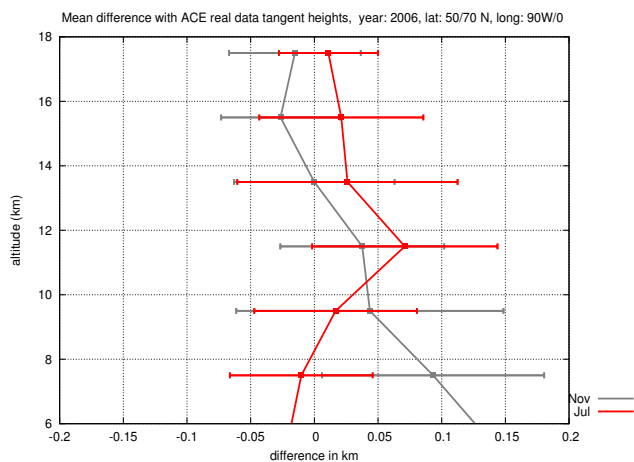


**Fig. 10.** Mean difference between N<sub>2</sub>-retrieved tangent height profiles and ACE v2.2 tangent heights from real occultation data for a region of the Northern Hemisphere (50–70° N; 0–90° W). The red curve represents the mean difference in July 2006 for 35 occultations. The grey curve represents the mean difference in November 2006 for 40 occultations. For each case, error bars correspond to the variance of the difference between ACE v2.2 tangent heights and N<sub>2</sub>-retrieved tangent heights for the selected set of occultations.

profiles and on tangent heights (as they are correlated in the case of real data), a simultaneous fit can markedly reduce these errors in comparison with single tangent heights retrieval. This is especially significant for our purpose when these errors are due to correlation with CO<sub>2</sub> a priori profile data.

### 5.1.2 First application to real data

These results are confirmed by looking at tangent height profiles retrieved from real ACE data for two months in 2006 (July and November). Figure 10 shows mean differences between N<sub>2</sub>-retrieved and ACE v2.2 tangent height profiles for these two months for a region of the Northern Hemisphere (50–70° N; 0–90° W). In July, the mean difference tangent height profile increases from –20 m to 75 m from 6 to 11 km and then decreases to +10 m at 18 km. In November the mean difference tangent height profile is different: it regularly decreases from +125 m at 6 km to –20 m at 18 km. At 6 km the difference between November and July is about 130 m while it is about 30 m at 18 km. ACE v2.2 tangent height errors due to correlation with CO<sub>2</sub> a priori profile are expected to be more important for lower altitudes because: (i) only CO<sub>2</sub> transitions are used to fit tangent heights below 12 km, and (ii) CO<sub>2</sub> seasonal variations are known to be more important at lower altitudes. ACE v2.2 tangent height retrieval sensitivity to CO<sub>2</sub> a priori concentration is of the order of 125 m for a 5 ppm change, a value which corresponds well to the change in CO<sub>2</sub> concentration between summer and autumn

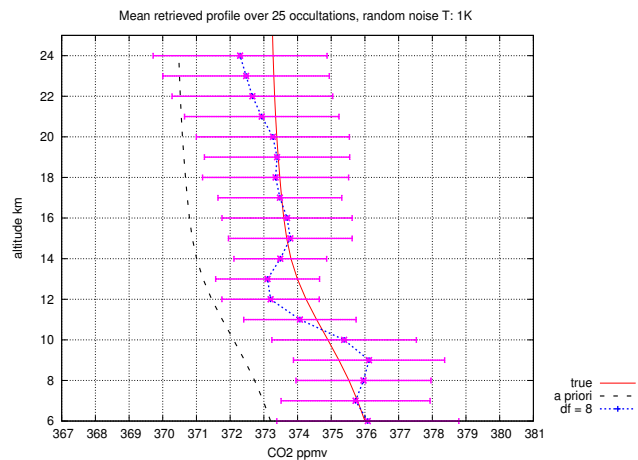


**Fig. 11a.** CO<sub>2</sub> mean retrieved profile averaged over 25 tests (blue) and empirical standard deviation of the sample (pink). The a priori profile (dotted dark) has a correct gradient sign. A 1 K noise has been added to the temperature profile. The true CO<sub>2</sub> profile is the red curve.

at 60° N in the middle troposphere (Bönisch, 2008; Engel, 2006). So, the difference observed in Fig. 10 may tentatively be explained by the seasonal CO<sub>2</sub> volume mixing ratio cycle not taken into account in the ACE v2.2 retrievals. This assumption has to be confirmed by extending the period of analysis. However, these test cases demonstrate that the tangent height retrieval using N<sub>2</sub> absorption instead of CO<sub>2</sub> lines is feasible also with real measurements. The variance observed of about 100 m throughout the altitude range in July and in November is consistent with previous synthetic results (see Sect. 5.1.1) and ACE v2.2 tangent height uncertainties.

## 5.2 CO<sub>2</sub> retrieval

### 5.2.1 Discussion of synthetic tests

CO<sub>2</sub> profiles are retrieved using the set of 25 CO<sub>2</sub> micro-windows selected in Sect. 3 and degrees of freedom between 8 and 9 corresponding to  $\alpha=10^{-3}$ . For the same assumed situation (same true profile and same a priori profile), CO<sub>2</sub> profiles are estimated for a total of 25 noise cases (1 K in temperature and a realistic random noise estimated from comparisons between true observations and synthetic calculations) and the results averaged. Results are first shown for two different assumed situations: in Fig. 11a, the a priori profile has the same gradient as the true profile with concentration values too low by about 3 ppm; in Fig. 11b, the a priori profile gradient has a sign opposite to that of the true profile with concentration values too large by about 2 ppm at 5 km and too low by about 3.5 ppm at 25 km. In these two cases, the error bars in pink correspond to “precision” (see Sect. 4.4) among the 25 retrievals. In Fig. 11a, from 5 to 15 km, the

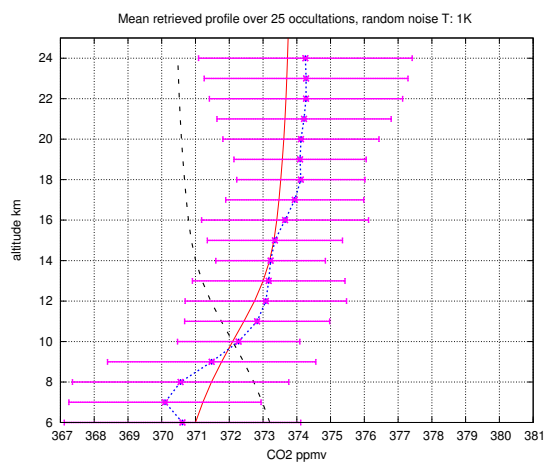


**Fig. 11b.** Same as Fig. 11a except using an a priori profile with a wrong gradient sign.

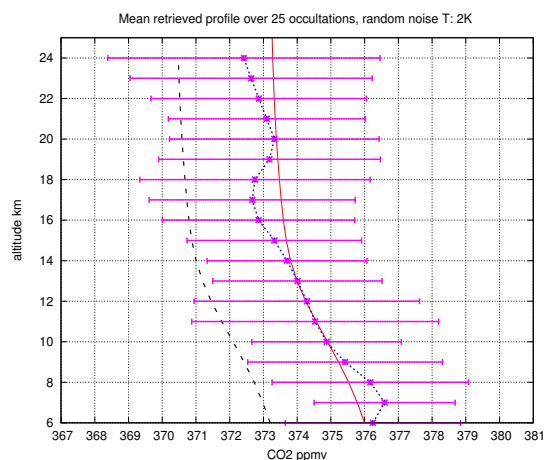


**Fig. 12.** Same as Fig. 11a with 2 K noise added to the temperature profile.

error bar value decreases from about 2.5 ppm to 1.5 ppm and then increases to 2.5 ppm to 25 km. In the case of the wrong a priori gradient of Fig. 11b, error bar values are larger by about 0.5 ppm with the same evolution with altitude (higher values at top and bottom of the altitude range). For the two cases (Fig. 11a and b) the maximum absolute difference with the true profile is about 1 ppm (due to spurious oscillations), and no significant bias due to the a priori profile appears. In Fig. 12, the same a priori and true profiles as Fig. 11a are used and a 2 K temperature random noise has been added to the temperature profile. The mean retrieved CO<sub>2</sub> profile using this noisy profile is represented in blue in the figure. The bias is still less than 1 ppm and error bar values increase by 1 ppm in comparison with Fig. 11a. Figure 13 considers the same case as Fig. 11a (only random noise on temperature

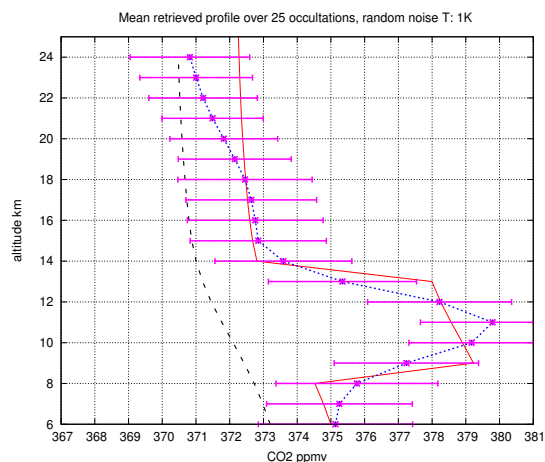


**Fig. 13.** Same as Fig. 11a with CO<sub>2</sub> with a true profile showing a 4–5 ppm “hump” in the 9–13 km altitude range.

profile) but the true profile (red) is shifted by 5 ppm in the 9–13 km altitude range from the previous true profile. The mean retrieved CO<sub>2</sub> profile (blue) follows quite well the true profile; the mean error is about 1 ppm and the mean dispersion is about 2 ppm. The two sharp steps from 13 to 14 km and from 8 to 9 km of the true profile “hump” are less accurately retrieved (maximum error of about 2.5 ppm). However, the retrieval can reproduce a 4 km thick CO<sub>2</sub> profile structure with a good vertical resolution. With the accuracy obtained on pointing parameters, assuming errors on the temperature profile of the order 1 K standard deviation, assuming instrumental and model noise according to ACE-FTS measurements, and assuming a regularization matrix based on the MOZART model CO<sub>2</sub> covariance matrix with degrees of freedom around 9, the retrieved CO<sub>2</sub> error averaged over 25 occultations comes to less than 1 ppm bias with a standard deviation around 2 ppm. This accuracy is consistent with the objectives described in Sect. 1 and validates the selection of CO<sub>2</sub> micro-windows (Table 3.2.1). The retrieval error due to MOZART CO<sub>2</sub> a priori profile is weak enough (less than 0.5 ppm) to allow averaging of spatially and temporally consistent retrieved CO<sub>2</sub> profiles.

## 5.2.2 First application to real data

Figure 14a and b display the first CO<sub>2</sub> profiles retrieved from ACE-FTS instrument in the 10–22 km altitude range. These profiles correspond to monthly means over the same Northern Hemisphere region (50–70° N; 0–90° W) for the months of July 2005 and 2006 (Fig. 14a) and November 2005 and 2006 (Fig. 14b). In each case, profiles correspond to averages over about 35 occultations. These figures correspond to CO<sub>2</sub> profiles retrieved using the isotopologue <sup>12</sup>C<sup>16</sup>O<sub>2</sub>. The mean standard deviation of the samples is around 2.5 ppm in all cases. An average increase of the CO<sub>2</sub> concentration from

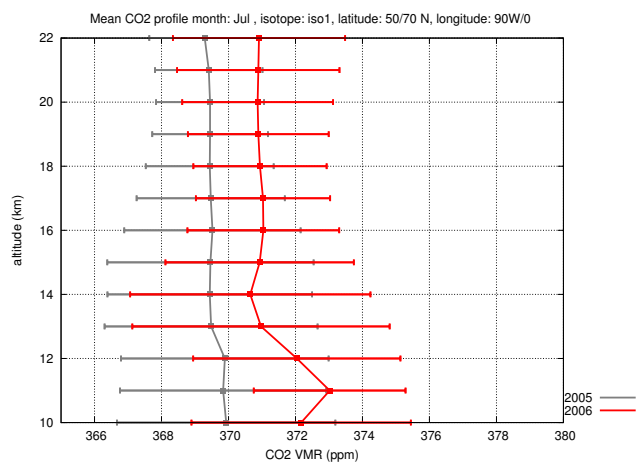


**Fig. 14a.** Mean retrieved CO<sub>2</sub> profile from real ACE data using 15 micro-windows of <sup>12</sup>C<sup>16</sup>O<sub>2</sub> in the 10–22 km altitude range for the same region as in Fig. 10 in the Northern Hemisphere. The red curve represents the mean CO<sub>2</sub> profile for July 2006 and grey curve corresponds to July 2005.

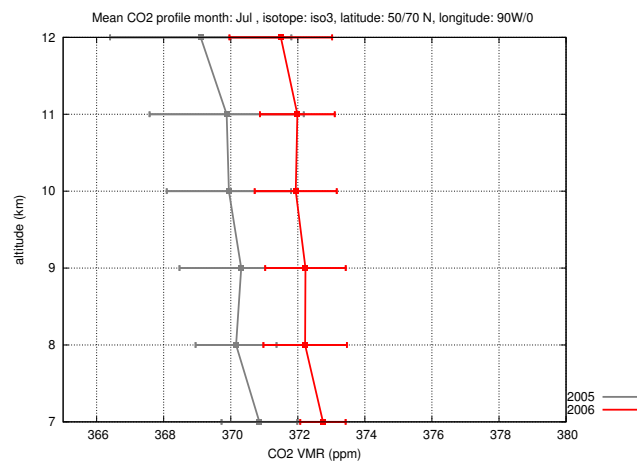


**Fig. 15a.** Mean retrieved CO<sub>2</sub> profile from real ACE data using 10 micro-windows of <sup>18</sup>OC<sup>16</sup>O in the 7–12 km altitude range for the same region as in Fig. 10 in the Northern Hemisphere. The red curve represents the mean CO<sub>2</sub> profile for July 2006 and grey curve corresponds to July 2005.

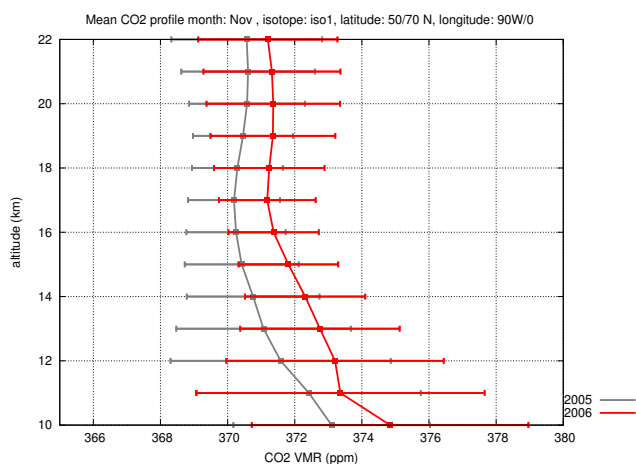


**Fig. 14b.** Same as Fig. 14a but in November 2005 and 2006.

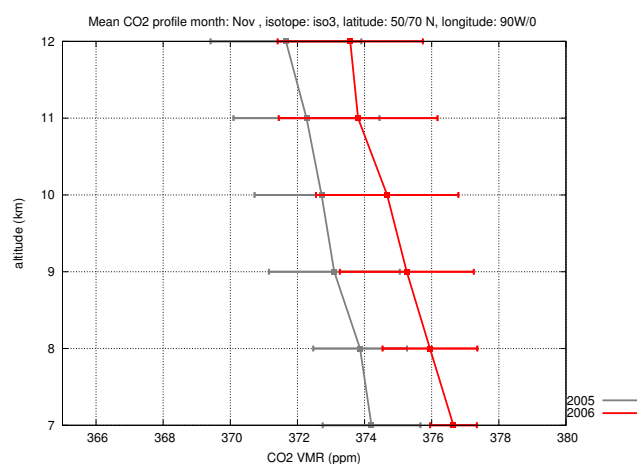


**Fig. 15b.** Same as Fig. 15a but in November 2005 and 2006.

2005 to 2006 of about 1.5–2 ppm is observed in good agreement with surface measurements: for example, +1.7 ppm in 2006 at Mauna Loa (see <http://www.esrl.noaa.gov/gmd/ccgg/trends>). In July (Fig. 14a), the CO<sub>2</sub> concentration is almost constant in 2005 and 2006 except a peak appearing in 2006 at 11 km. From 10 to 22 km, a negative gradient of about 0.5 ppm in 2005 and 1 ppm in 2006 is observed. In November (Fig. 14b), a negative gradient from 10 to 22 km of about 3 ppm is seen in 2005 and of 4 ppm in 2006. Isotopologue <sup>18</sup>OC<sup>16</sup>O is suitable for retrieving profiles for lower altitudes and results are shown on Fig. 15a (July) and Fig. 15b (November), for the altitude range 7–12 km. These results show a mean standard deviation around 1.5 ppm, signifi-

cantly better than for the previous cases due to the robustness of these transitions to temperature. These profiles have been made consistent with those obtained from <sup>12</sup>C<sup>16</sup>O<sub>2</sub> transitions by multiplying the retrieved concentration by 0.967 in July and 0.973 in November, a scaling factor close to the one found by Boone (2005) who explains that this discrepancy could be a result of systematic errors in the strengths of <sup>18</sup>OC<sup>16</sup>O lines and/or an actual physical difference in the mixing ratio from the expected <sup>12</sup>C<sup>16</sup>O<sub>2</sub> to <sup>18</sup>OC<sup>16</sup>O isotopic ratio. Figure 15a shows CO<sub>2</sub> profiles in July 2005 and 2006 for the 7–12 km altitude range; the increase of the mixing ratio is still of about 2 ppm and the vertical negative gradient from 7 to 12 km is about 1 ppm in 2005 and 2006. The peak

seen at 11 km on Fig. 14a is not seen here. Figure 15b shows CO<sub>2</sub> profiles in November 2005 and 2006 for the same altitude range; the mixing ratio again increases by about 2 ppm and the vertical negative gradients are close to the one observed on Fig. 14b. In conclusion, these preliminary results obtained from real occultations show a CO<sub>2</sub> concentration trend close to the one measured in situ and a vertical gradient in July and November consistent with aircraft measurement campaigns (Engel, 2006; Sawa, 2008).

## 6 Conclusions and future work

Accurate temporal and spatial determination of CO<sub>2</sub> concentration profiles is of great importance for the improvement of air transport models. Coupled with column measurements from a nadir instrument, occultation measurements will also bring useful constraints to the surface carbon flux determination (Pak, 2001; Patra, 2003), for example, by indicating what portion of the column measurement comes from the region below 5 km.

In this paper we have shown that, in contrast to present and near future satellite observations of the distribution of CO<sub>2</sub>, which provide vertically integrated concentrations, the high spectral resolution and signal to noise ratio of the solar occultation measurements of the ACE-FTS instrument on board SCISAT are able to provide CO<sub>2</sub> vertical profiles in the 5–25 km altitude range. The major difficulty, when applying a conventional method where the tangent heights pointing information is retrieved from CO<sub>2</sub> transitions is the correlation which exists between the pointing parameters (tangent heights of measurements and temperature profiles) and a CO<sub>2</sub> a priori profile in this altitude range. This problem has been solved using, for the first time, the N<sub>2</sub> collision-induced absorption continuum near 2500 cm<sup>-1</sup>. Its high sensitivity to altitude leads to an estimated precision less than 100 m for the tangent height N<sub>2</sub>-retrieval. These results are confirmed by first retrievals from real ACE-FTS data. Moreover, in the 5–25 km altitude range, the selection of CO<sub>2</sub> lines with low values of the lower state energy value  $E''$  makes the CO<sub>2</sub> retrieval quite insensitive to temperature uncertainties. A comprehensive analysis of the errors (estimated from real data) introduced by the instrument, spectroscopy, interfering species, and temperature has resulted in the selection of a set of 25 CO<sub>2</sub> micro-windows. The use of an optimized regularization matrix based on a CO<sub>2</sub> covariance matrix calculated from the MOZART model ensures good convergence of the non-linear iterative retrieval method with an acceptable number of degrees of freedom and a vertical resolution around 2 km. The estimated CO<sub>2</sub> total error shows a bias of about 1 ppm with a standard deviation of about 2 ppm after averaging over 25 spatially and temporally consistent profiles. These synthetic results, simulating realistic conditions of observation, and the first CO<sub>2</sub> vertical profiles retrieved from real occultations shown in this paper are very encour-

aging as they basically match our present knowledge. The method will soon be applied to the whole ACE-FTS archive providing, for the first time, CO<sub>2</sub> vertical profiles in the 5–25 km altitude range over a period of more than 4 years on a near global scale.

One remaining issue that will need to be solved is the use of <sup>18</sup>OC<sup>16</sup>O lines near 2610 cm for the lowest altitudes and <sup>13</sup>C<sup>16</sup>O<sub>2</sub> lines near 2020 cm in the retrieval. The ratio of isotopologues concentrations in the atmosphere can vary from the standard abundance value assumed for the line intensities in the spectroscopic databases, especially the ratio of <sup>18</sup>OC<sup>16</sup>O to <sup>12</sup>C<sup>16</sup>O<sub>2</sub> concentration. However, the consistency seen between profiles retrieved from real data using either <sup>18</sup>OC<sup>16</sup>O lines for the 7–12 km altitude range or <sup>12</sup>C<sup>16</sup>O<sub>2</sub> lines for the 10–22 km is very encouraging.

*Acknowledgements.* We gratefully acknowledge R. Armante, C. Crevoisier, B. Legras and N. A. Scott for fruitful discussions, help and constructive criticisms.

The ACE mission is supported primarily by the Canadian Space Agency (CSA) and some support was provided by the Natural Environment Research Council (NERC) of the UK.

Edited by: R. Sander



The publication of this article is financed by CNRS-INSU.

## References

- Anderson, B., Gregory, G., Collins, J. J., Sachse, G., Conway, T., and Whiting, G.: Airborne observations of spatial and temporal variability of tropospheric carbon dioxide, *J. Geophys. Res.*, 101, 1985–1997, 1996.
- Andrew, A. E., Boering, K. A., Daube, B. C., Wofsy, S. C., Loewenstein, M., Jost, H., Podolske, J. R., Webster, C. R., Herman, R. L., Scott, D. C., Flesch, G. J., Moyer, E. J., Elkins, J. W., Dutton, G. S., Hurst, D. F., Moore, F. L., Ray, E. A., Romashkin, P. A., and Strahan, S. E.: Mean ages of stratospheric air derived from in situ observations of CO<sub>2</sub>, CH<sub>4</sub>, and N<sub>2</sub>O, *J. Geophys. Res.*, 106, 32295–32314, 2001.
- Baker, D. F., Law, R. M., Gurney, K. R., Rayner, P., Peylin, P., Denning, A. S., Bousquet, P., Bruhwiler, L., Chen, Y. H., Ciais, P., Fung, I. Y., Heimann, M., John, J., Maki, T., Maksyutov, S., Masarie, K., Prather, M., Pak, B., Taguchi, S., and Zhu, Z.: TransCom3 inversion intercomparison: Interannual variability of regional CO<sub>2</sub> fluxes, *Global Biogeochem. Cy.*, 1988–2003, doi:10.1029/2004GB002439, 2006.
- Bernath, P. F.: Atmospheric Chemistry Experiment (ACE): Analytical Chemistry from Orbit, *Trends Anal. Chem.*, 25, 647–654, 2006.

- Bernath, P. F., McElroy, C. T., Abrams, M. C., Boone, C. D., Butler, M., Camy-Peyret, C., Carleer, M., Clerbaux, C., Coheur, P.-F., Colin, R., DeCola, P., DeMaziere, M., Drummond, J. R., Dufour, D., Evans, W. F. J., Fast, H., Fussen, D., Gilbert, K., Jennings, D. E., Llewellyn, E. J., Lowe, R. P., Mahieu, E., McConnel, J. C., McHugh, M., McLeod, S. D., Michaud, R., Midwinter, C., Nassar, R., Nichitiu, F., Nowland, C., Rinsland, C. P., Rochon, Y. J., Rowlands, N., Semeniuk, K., Simon, P., Skelton, R., Sloan, J. J., Soucy, M. A., Strong, K., Tremblay, P., Turnbull, D., Walker, K. A., Walkty, I., Wardle, D. A., Wehrle, V., Zander, R., and Zou, T.: Atmospheric Chemistry Experiment (ACE): Mission overview, *Geophys. Res. Lett.*, 32, L15S01, doi:10.1029/2005GLO22386, 2005.
- Bönisch, H., Hoor, P., Gurk, C., Feng, W., Chipperfield, M., Engel, A., and Bregman, B.: Model evaluation of CO<sub>2</sub> and SF<sub>6</sub> in the extratropical UT/LS region, *J. Geophys. Res.*, 113, D06101, doi:10.1029/2007JD008829, 2008.
- Boone, C. D., Nassar, R., Walker, K. A., Rochon, Y., McLeod, S. D., Rinsland, C. P., and Bernath, P. F.: Retrievals for the Atmospheric Chemistry Experiment Fourier-Transform Spectrometer, *Appl. Opt.*, 44, 7218–7231, 2005.
- Brenninkmeijer, C. A. M., Crutzen, P. J., Fischer, H., Gsten, H., Hans, W., Heinrich, G., Heintzenberg, J., Hermann, M., Immelmann, T., Kersting, D., Maiss, M., Nolle, M., Pitscheider, A., Pohlkamp, H., Scharffe, D., Specht, K., and Wiedensohler, A.: CARIBIC: Civil Aircraft for Global Measurement of Trace Gases and Aerosols in the Tropopause Region, *J. Atmos. Ocean. Tech.*, 16, 1373–1383, 1999.
- Buchwitz, M., de Beek, R., Noel, S., Burrowsand, J. P., Bovensmann, H., Bremer, H., Bergamaschi, P., Krner, S., and Heimann, M.: Carbon monoxide, methane and carbon dioxide columns retrieved from SCIAMACHY by WFM-DOAS: year 2003 initial data set., *Atmos. Chem. Phys.*, 5, 3313–3329, 2005, <http://www.atmos-chem-phys.net/5/3313/2005/>.
- Chédin, A., Serrar, S., Armante, R., Scott, N. A., and Hollingsworth, A.: Signatures of annual and seasonal variations of CO<sub>2</sub> and other greenhouse gases from comparisons between NOAA/TOVS observations and model simulations, *J. Clim.*, 15, 95–116, 2002.
- Chédin, A., Serrar, S., Scott, N. A., Crevoisier, C., and Armante, R.: First global measurement of mid-tropospheric CO<sub>2</sub> from NOAA polar satellites: the tropical zone, *J. Geophys. Res.*, 108, 4581, doi:10.1029/2003JD003439, 2003a.
- Chédin, A., Saunders, R., Hollingsworth, A., Scott, N. A., Matricardi, M., Etcheto, J., Clerbaux, C., Armante, R., and Crevoisier, C.: The feasibility of monitoring CO<sub>2</sub> from high-resolution infrared sounders, *J. Geophys. Res.*, 108, 4064, doi:10.1029/2001JD001144, 2003b.
- Crevoisier, C., Heilliette, S., Chédin, A., Serrar, S., Armante, R., and Scott, N. A.: Midtropospheric CO<sub>2</sub> concentration retrieval from AIRS observations in the tropics, *Geophys. Res. Lett.*, 31, L17106, doi:10.1029/2004GL020141, 2004.
- Dudhia, A., Jay, V. L., and Rodgers, C. D.: Microwindow selection for high-spectral-resolution sounders, *Appl. Opt.*, 41, 3665–3673, 2002.
- Engel, A., Bönisch, H., Brunner, D., Fischer, H., Franke, H., Gunter, G., Gurk, C., Hegglin, M., Hoor, P., Königstedt, R., Krebach, M., Maser, R., Parchatka, U., Peter, T., Schell, D., Schiller, C., Schmidt, U., Spelten, N., Szabo, T., Weers, U., Wernli, H., Wetter, T., and Wirth, V.: Highly resolved observations of trace gases in the lowermost stratosphere from the Spurt project: an overview, *Atmos. Chem. Phys.*, 6, 283–301, 2006, <http://www.atmos-chem-phys.net/6/283/2006/>.
- Engelen, R. J. and McNally, A. P.: Estimating atmospheric CO<sub>2</sub> from advanced infrared satellite radiances within an operational four-dimensional variational (4D-Var) data assimilation system: Results and validation, *J. Geophys. Res.*, 110, D18305, doi:10.1029/2005JD005982, 2005.
- Gelb, A.: *Applied Optimal Estimation*, M.I.T. Press, 180–229, 1974.
- Gurney, K. R., Law, R. M., Denning, A. S., Rayner, P. J., Baker, D., Bousquet, P., Bruhwiler, L., Chen, Y. H., Ciais, P., Fan, S., Fung, I. Y., Gloor, M., Heimann, M., Higuchi, K., John, J., Maki, T., Maksyutov, S., Masarie, K., Peylin, P., Prather, M., Pak, B. C., Randerson, J., Sarmiento, J., Taguchi, S., Takahashi, T., and Yuen, C. W.: Towards robust regional estimates of CO<sub>2</sub> sources and sinks using atmospheric transport models, *Nature*, 415, 626–630, 2002.
- Hegglin, M. I., Boone, C. D., Manney, G. L., Shepherd, T. G., Walker, K. A., Bernath, P. F., Daffer, W. H., Hoor, P., and Schiller, C.: Validation of ACE-FTS satellite data in the upper troposphere/lower stratosphere (UTLS) using non-coincident measurements, *Atmos. Chem. Phys.*, 8, 1483–1499, 2008, <http://www.atmos-chem-phys.net/8/1483/2008/>.
- Horowitz, L. W., Walters, S., Mauzerall, D. L., Emmons, L. K., Rasch, P. J., Granier, C., Tie, X., Lamarque, J. F., Schultz, M. G., Tyndall, G. S., Orlando, J. J., and Brasseur, G. P.: A global simulation of tropospheric ozone and related tracers: Description and evaluation of MOZART, version 2, *J. Geophys. Res.*, 108, 4784, doi:10.1029/2002JD002853, 2003.
- Jacquinet-Husson, N., Scott, N. A., Chédin, A., Crépeau, L., Armante, R., Capelle, V., Orphal, J., Coustenis, A., Boone, C., Poulet-Crovisier, N., Barbe, A., Birk, M., Brown, L. R., Camy-Peyret, C., Claveau, C., Chance, K., Christidis, N., Clerbaux, C., Coheur, P. F., Dana, V., Daumont, L., Backer-Barilly, M. R. D., Lonardo, G. D., Flaud, J. M., Goldman, A., Hamdouni, A., Hess, M., Hurley, M. D., Jacquemart, D., Kleiner, I., Kpke, P., Mandin, J. Y., Massie, S., Mikhailenko, S., Nemtchinov, V., Nikitin, A., Newnham, D., Perrin, A., Perevalov, V., Pinnock, S., Rgalia-Jarlot, L., Rinsland, C., Rublev, A., Schreier, F., Schult, L., Smithu, K. M., Tashkun, S. A., Teffo, J. L., Toth, R. A., Tyuterev, V. G., Auwera, J. V., Varanasi, P., and Wagner, G.: The GEISA spectroscopic database: Current and future archive for Earth and planetary atmosphere studies, *JQSRT*, 100, 1043–1059, 2008.
- Koner, P. K. and Drummond, J. R.: Atmospheric trace gases profile retrievals using the nonlinear regularized total least square method, *JQSRT*, 109, 2045–2059, doi:10.1016/j.jqsrt.2008.02.014, 2008.
- Lafferty, W. J., Solodov, A. M., Weber, A., Olson, W. B., and Hartmann, J.-M.: Infrared collision-induced absorption by N<sub>2</sub> near 4.3 μm for atmospheric applications: measurements and empirical modeling, *Appl. Opt.*, 35, 5911–5917, 1996.
- Levenberg, K.: A Method for the Solution of Certain Non-Linear Problems in Least Squares. *The Quarterly of Applied Mathematics*, 2, 164–168, 1944.
- Matsueda, H., Taguchi, S., Inoue, H. Y., and Ishii, M.: A large impact of tropical biomass burning on CO and CO<sub>2</sub> in the upper

- troposphere, *Science China Press*, 45, 116–125, 2002.
- Marquardt, D.: An Algorithm for Least-Squares Estimation of Nonlinear Parameters. *SIAM J. Appl. Math.*, 11, 431–441, doi:10.1137/0111030, 1963.
- Olsen, S. C. and Randerson, J. T.: Differences between surface and column atmospheric CO<sub>2</sub> and implications for carbon cycle research, *J. Geophys. Res.*, 109, D02301, doi:10.1029/2003JD003968, 2004.
- Pak, B. C. and Prather, M. J.: CO<sub>2</sub> source inversions using satellite observations of the upper troposphere, *Geophys. Res. Lett.*, 28, 4571–4574, 2001.
- Park, J. H.: Atmospheric CO<sub>2</sub> monitoring from space, *Appl. Opt.*, 36, 2701–2712, 1997.
- Patra, P. K., Maksyutov, S., Sasano, Y., Nakajima, H., Inoue, G., and Nakazawa, T.: An evaluation of CO<sub>2</sub> observations with Solar Occultation FTS for Inclined-Orbit Satellite sensor for surface source inversion, *J. Geophys. Res.*, 108(D24), 4759, doi:10.1029/2003JD003661, 2003.
- Phillips, D. L.: A Technique for the Numerical Solution of Certain Integral Equations of the First Kind, *J. Assoc. Comput. Mach.*, 9, 84–97, 1962.
- Plumb, R.: A “tropical pipe” model of stratospheric transport, *J. Geophys. Res.*, 301, 3957–3972, 1996.
- Plumb, R. and Ko, M.: Interrelationships between mixing ratios of long-lived stratosphere constituents, *J. Geophys. Res.*, 97, 10145–10156, 1992.
- Rodgers, C. D.: Inverse methods for atmospheric sounding. Theory and practice, World scientific, Singapore, 90–98, 2000.
- Sawa, Y., Machida, T. and Matsueda, H.: Seasonal variations of CO<sub>2</sub> near the tropopause observed by commercial aircraft, *J. Geophys. Res.*, 113, D23301, doi:10.1029/2008JD010568, 2008.
- Scott, N. A.: A direct method of computation of transmission function of an inhomogeneous gaseous medium : description of the method and influence of various factor, *JQSRT*, 14, 691–707, 1974.
- Scott, N. A. and Chédin, A.: A fast line-by-line method for atmospheric absorption computation: The Automatized Atmospheric Absorption Atlas, *J. Appl. Meteorol.*, 20, 801–812, 1981.
- Shia, R. L., Liang, M. C., Miller, C. E., and Yung, Y. L.: CO<sub>2</sub> in the upper troposphere: Influence of stratospheretroposphere exchange, *Geophys. Res. Lett.*, 33, L1481, doi:10.1029/2006GL026141, 2006.
- Steck, T.: Methods for determining regularization for atmospheric retrieval problems, *Appl. Opt.*, 41, 1788–1797, 2002.
- Tikhonov, A. N.: On the regularization of ill-posed problems. *Dokl. Akad. Nauk SSSR*, 153, 49–52; *MR*, 28, 5577; *Soviet Math. Dokl.*, 4, 1624–1627, 1963.
- Twomey, S.: On the Numerical Solution of Fredholm Integral Equations of the First Kind by the Inversion of the Linear System Produced by Quadrature, *J. Assoc. Comp. Mach.*, 10, 97–101, 1963.
- von Clarmann, T. and Echle, G.: Selection of optimized microwindows for atmospheric spectroscopy, *Appl. Opt.*, 37, 7661–7669, 1998.
- von Clarmann, T., Glatthor, N., Grabowski, U., Hopfner, M., Kellmann, S., Kiefer, M., Linden, A., Tsidu, G. M., Milz, M., Steck, T., Stiller, G. P., Wang, D. Y., Fischer, H., Funke, B., and Gil-López-Puerta, S.: Retrieval of temperature and tangent altitude pointing from limb emission spectra recorded from space by the Michelson Interferometer for Passive Atmospheric Sounding (MIPAS), *J. Geophys. Res.*, 108, 4736–4750, 2003.